JTTEE5 17:60–72
DOI: 10.1007/s11666-007-9140-6
1059-9630/$19.00 © ASM International

Peer Reviewed

Fluid Mechanics and Heat Transfer of Liquid Precursor Droplets Injected into High-Temperature Plasmas

Saptarshi Basu, Eric H. Jordan, and Baki M. Cetegen

(Submitted January 26, 2007; in revised form May 14, 2007)

Thermo-physical processes in liquid ceramic precursor droplets in plasma were modeled. Models include aerodynamic droplet break-up, droplet transport, as well as heat and mass transfer within individual droplets. Droplet size, solute concentration, and plasma temperature effects are studied. Results are discussed with the perspective of selecting processing conditions and injection parameters to obtain certain types of coating microstructures. Small droplets (<5 microns) are found to undergo volumetric precipitation and coating deposition with small unpyrolized material. Droplets can be made to undergo shear break-up by reducing surface tension and small droplets promote volumetric precipitation. Small particles reach substrate as molten splats resulting in denser coatings. Model predicts that larger droplets (>5 microns) tend to surface precipitate-forming shells with liquid core. They may be subjected to internal pressurization leading to shattering of shells and secondary atomization of liquid within. They arrive at the substrate as broken shells and unpyrolized material.

Keywords influence of process parameters, plasma spray forming, spray deposition, TS coating process

1. Introduction

Plasma thermal spray processes are commonly employed to generate functional coatings on hardware components. Typical thermal spray process involves injection of particles into a high-temperature plasma jet and their deposition onto a component surface following melting and re-solidification. Depending on the processing conditions, different coating microstructures can be obtained in thermal spray processes (Ref 1, 2). In a different approach, injection of a liquid spray or stream containing ceramic precursor salts has been pursued with successful results (Ref 3-8). This process, now commonly referred to as Solution Precursor Plasma Spray (SPPS) process, has gained significant interest due to the relative ease of liquid injection into the plasma as compared to powder feeding and the possibilities of different compositions and in situ composition variations. As in any thermal spray process, a detailed understanding of various thermophysical and thermochemical transformations of precursor injected into the plasma is required in order to improve the design and control of the spraying process. Some of these processes include droplet shear break-up, evaporative shrinkage, and precipitation of dissolved solute resulting in different particle morphologies. The chemical, thermal, and morphological states of the plasma-processed precursor droplets ultimately determine the coating microstructure and its macroscopic properties. Parameters such as droplet size, injection velocity, location and temperature zone of plasma where droplets are injected, precursor characteristics, plasma temperature, and velocity fields can all have varying influences on the final outcome.

Figure 1 shows various possible processing paths for liquid precursor droplets leading to different in-flight particle morphologies. Depending on the heating rate, droplet size and properties of the dissolved solute, precipitation characteristics can vary significantly leading to particle morphologies from solid particles to hollow spheres and fragmented shells produced by internal pressurization and particle rupture. Small droplets experience a more uniform increase in solute concentration throughout the droplet during the evaporation phase leading to volume precipitation and solid particle morphology as indicated in Fig. 1a. For larger sized droplets or solutes having low super-saturation limit, shell formation occurs due to surface precipitation and shell formation as indicated in Fig. 1b. This path can have different final morphologies depending on the porosity of the formed shell. For low porosity shells (path I), internal pressurization due to vaporization of the trapped liquid by further heating causes shell fracture. For impervious shell (Path III), not only fragmentation but also secondary atomization from the liquid core may be experienced. For highly permeable shells (Path II), there may be sufficient venting to counteract the pressure rise and hence hollow shells may be formed. For some precursors, the formed shell may be elastic and the subsequent internal

Saptarshi Basu, Eric H. Jordan, and **Baki M. Cetegen**, Department of Mechanical Engineering, University of Connecticut, Storrs, CT 06269-3139. Contact e-mail: cetegen@engr.uconn.edu.

Nomenclature

C_D	Drag coefficient
$C_{p,d}$	Specific heat
D_{12}	Mass diffusivity of the vapor phase into plasma
D_s	Mass diffusivity of Zirconium acetate into water
h_{lv}	Latent heat of vaporization for liquid
k	Thermal conductivity
Le	Lewis number, $\mathrm{Le} = D/\alpha$
$\dot{m}$	Mass flow rate at the droplet surface due to vaporization
Pr	Prandtl number, $\mathrm{Pr} = \nu/\alpha$
$\dot{Q}_L$	Heat transfer rate into the droplet surface
r_s	Instantaneous outer radius of the droplet
$\bar{r}_s$	Non-dimensional radius of the droplet, $\bar{r}_s = r_s/r_0$
Re_d	Reynolds number based on droplet radius and relative velocity between the plasma and droplet
Nu	Nusselt number
t	Time
T	Temperature
$\bar{T}$	Nondimensional temperature, $\bar{T} = (T - T_0)/T_0$
U	Axial velocity of the droplet
U_∞	Axial plasma velocity
T_d	Droplet temperature in Eq 5
r_l	Radius of the liquid core
δ	Thickness of the shell
V_{pore}	Velocity of vapor venting through the pore
A_{pore}	Total area of the pores
χ	Mass fraction in the before precipitation regime
χ_s	Mass fraction in the liquid core after precipitation regime
$\bar{\chi}$	Nondimensional mass fraction, $\bar{\chi} = (\chi - \chi_0)/\chi_0$
η	Nondimensional radial coordinate, $\eta = r/r_s$
ν	Kinematic viscosity
μ	Dynamic viscosity
ρ	Density
τ	Nondimensional time, $\tau = \alpha_L t/r_0^2$
σ	Yield stress
p_v	Vapor pressure inside the solid shell
p_∞	Pressure outside the droplet
d	Diameter of the droplets in Eq 5 and 6
R	Universal gas constant
h	Coefficient of heat transfer in Eq 5 and 6

Subscript

0	Initial value
l	Liquid phase
v	Vapor phase
∞	Far field
d	Droplet in Eq 4-6
p	Plasma in Eq 4

pressurization results in inflation and rupture of the shell into collapsed precipitate clump. This is shown in Fig. 1c.

Experimental study of droplet/particle level processes in a plasma is extremely difficult and often impossible due to turbulent, very high temperature and velocity environment in plasmas employed in thermal spray systems. While progress has been made in measurement of plasma temperature and velocity fields by optical techniques, particle/droplet size, velocity, and temperature measurements are at best qualitative. Recently, Oberste-Berghaus et al. (Ref 9) described an optical technique for measuring temperature and velocity of small droplets in plasmas. Other types of characterization at the particle/droplet level involves extractive sampling and ex situ characterization by SEM. Most of these measurements are not able to shed light on the various processes within the droplet scale; thus, modeling is the only viable approach to explore these processes at the droplet level.

Comprehensive modeling of precursor droplets injected into a high-temperature plasma has been undertaken relatively recently. Ozturk and Cetegen (Ref 10-12) provided a complete physical description of single droplet vaporization for droplets convecting in high-temperature plasma or oxy-fuel combustion jets. Castillo and Munz (Ref 13) had undertaken detailed modeling of droplets injected into an RF plasma. Early studies by Fuchs (Ref 14) and Ranz and Marshall (Ref 15) included analytical studies of diffusion and evaporation in droplets. Due to the limitations of these studies such as constant droplet diameter during evaporation, more detailed solutions of droplet

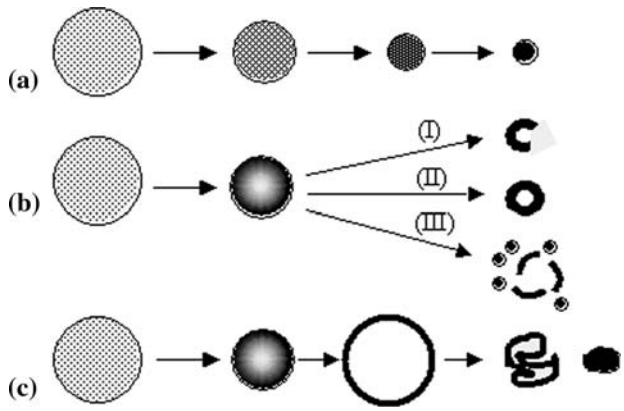

Fig. 1 Solute containing droplet vaporization and precipitation routes: (a) Uniform concentration of solute and volume precipitation leading to solid particles; (b) supersaturation near the surface followed by (I) fragmented shell formation (low permeability through the shell, (II) unfragmented shell formation (high permeability), (III) impermeable shell formation, internal heating, pressurization and subsequent shell break-up, and secondary atomization from the internal liquid; (c) elastic shell formation, inflation, and deflation by solids consolidation

vaporization, and the resulting solute concentration fields were obtained from numerical analysis (Ref 16). Most of these studies only considered droplets vaporizing in a surrounding high-temperature stagnant gas environment.

In this article, a series of models are presented to determine the importance and outcome of the

thermo-physical processes that take place in plasma processing of precursor droplets. In the following, models for aerodynamic droplet break-up, vaporization and solute precipitation, and internal pressurization and rupture of the formed precipitate shell formations are discussed. The results of these models are presented and discussed in the context of the relationship between the formed particle morphologies and coating microstructural characteristics. The work presented in this paper emphasizes three important phenomena associated with SPPS processes namely aerodynamic break-up, precipitation, and internal pressurization. To the best knowledge of the authors, these important phenomena have not been studied collectively to portray a complete picture of the entire lifetime of the droplet from injection to deposition on the substrate. In this article, we attempt to emphasize the relative importance and sequence of each of these phenomena along with their associated timescales.

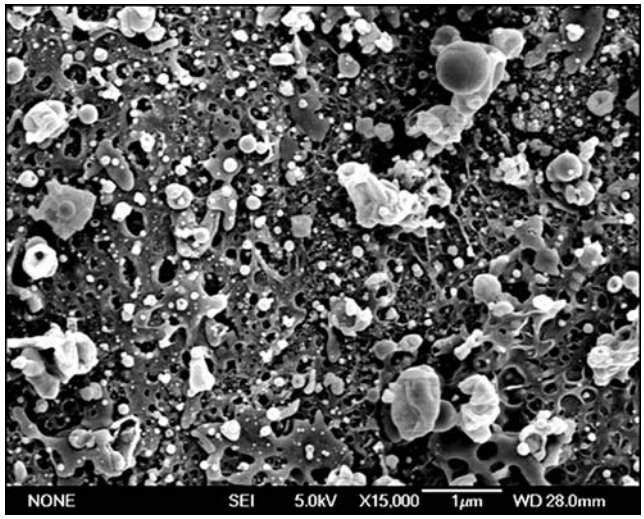

Fig. 2 SEM image of the deposition on a substrate after a single pass. Evidence of solid molten mass and cracked shells are visible on the substrate

2. Droplet Processes in a Plasma Jet

The processes that the droplets undergo after being injected axially or transversely into a high-temperature plasma can be divided into three distinct phases. The first is the aerodynamic break-up as slow moving droplets are entrained into the high-velocity plasma jet resulting in shear forces around the droplets. Depending on the size and thermo-physical properties, the droplets can undergo severe deformation and eventually break-up into smaller droplets. The timescale associated with this process is of the order of microseconds. The key parameters responsible for the aerodynamic break-up and deformation are the droplet size, relative velocity between the droplet and the plasma as well as the surface tension. It is usually found that larger droplets with low surface tension undergo break-up. The droplet break-up process in the plasma can be important for obtaining high-density durable coatings by plasma spraying, as will be discussed later.

The second phase is droplet heating and surface evaporation in the hot plasma jet stream. Loss of solvent from the surface concentrates the salt solutes progressively leading to precipitation of the solute as it reaches a supersaturation level and engulfs all regions of the droplet that exceed the equilibrium saturation concentration according to homogeneous precipitation hypothesis (Ref 17). Depending on the droplet size and the mass transport characteristics within the droplet, different precipitate morphologies can be obtained. Shell type morphologies and spherical precipitates are possible. While thickness of the shell can be predicted from the homogeneous nucleation hypothesis, the porosity is not at all predictable. Indirect evidence of shell formation has been found in the spray pyrolysis literature where the heating rate is much lower than in a plasma. Both types of morphologies have been found in plasma processing of liquid precursors as shown in Fig. 2. Several fundamental studies regarding the morphology of particle structure have been reported in the literature. These studies, however, were restricted to slower heating rates encountered in spray pyrolysis. Nevertheless, the results reported by Zhang et al. (Ref 18), Jain et al. (Ref 19), and Che et al. (Ref 20) show that different shell structures and morphology were obtained based on reactions within the droplet and the solute properties. Linn and Gentry (Ref 21) performed a detailed precipitation analysis of a single droplet prepared from different aqueous solutions like sodium acetate, calcium acetate, etc. They found that even for low heating rates as in spray pyrolysis, phenomena like evaporative droplet shrinkage, crust formation due to precipitation and subsequent fracture were all distinctly evident. The morphology of the crust depended on the solution type. The extensive work in the literature (Ref 18-21) as well as our experimental findings (Ref 4-6) in plasma spraying process indicate that precipitation kinetics is a multiparameter-dependent variable which is hard to correlate even under carefully controlled heating conditions. The hypothesis of homogeneous nucleation as is used in the current model and previous works is at best an ad hoc one with no firm experimental backing. It is, however, prudent to use sudden precipitation criteria based on a preset solute concentration as a qualitative estimate of the actual precipitation. While this estimate is not accurate and does not capture the intricacies of the kinetics leading to crust formation, its usefulness lies in designing spray processes based on semirealistic models rather than expensive and time-consuming trial and error experimentation.

The third phase is the further heating of the precipitates in the plasma before their impact on the substrate surface. In addition to the chemical transformation of the precipitate into ceramics, thermo-physical processes include vaporization of the liquid in the core for shell type precipitates, vapor venting from porous shell, pressure build-up within the shell, and possible shell rupture. These processes are dependent on the formed shell thickness, heating rate in the plasma, and porosity level. All three

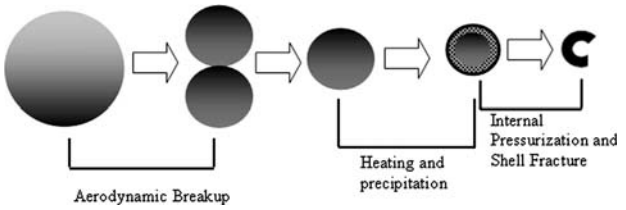

Fig. 3 The three phases of the thermal history of droplet injected in the plasma

stages of the droplet processes are shown schematically in Fig. 3. Modeling approaches for each stage are described in the following sections.

2.1 Initial Stage of Aerodynamic Break-up

Aerodynamic break-up is the first possible physical transformation a droplet undergoes as soon as it is injected into the plasma. The precursor droplets can be injected transversely or axially into the plasma, although transverse injection is the most common way of injecting droplets and particulates into a DC-arc plasma. The injected droplets experience high-velocity plasma gas and aerodynamic shear on the droplet surface. The flow-induced shear gives rise to a variety of instabilities depending on the droplet size and thermo-physical properties leading to deformation and break-up.

The factors influencing the droplet break-up are the relative velocity between the droplet and surrounding flow, damping forces due to viscosity, and surface tension. Other effects like surface evaporation is usually considered to be negligible at the timescale of the droplet break-up process. Relative inertial, viscous and surface tension forces can be written as,

$$F_{\text{inertia}} \propto m_{\text{d}} \frac{2\rho_{\text{p}}(\Delta u)^2}{\rho_{\text{d}} d}, \quad F_{\text{viscous}} \propto \mu_{\text{d}} \dot{x} d, \quad F_{\text{ST}} \propto \sigma x \tag{Eq 1}$$

where ρ_{p} is the density of the plasma jet, Δu is the relative velocity between the droplet and plasma gas, d is droplet diameter, μ_{d} is the dynamic viscosity of the droplet, and x and $\dot{x}$ are the distortion and the distortion rate of the droplet from the spherical shape, and σ is the surface tension. A large droplet injected with a velocity of approximately 12-15 m/s into the hot plasma jet of velocity of 600 m/s experiences a very large inertial force and distort from their spherical shape. Viscous damping and surface tension forces help dampen the droplet distortion. The relevant nondimensional parameter to enunciate the relative importance of the inertia and surface tension is the Weber number defined as,

$$We = \frac{\rho_{\text{p}}(\Delta u)^2 d}{\sigma} \tag{Eq 2}$$

Values of Weber number greater than unity suggest that inertia forces are more important than the surface tension and hence the droplets are prone to deformation and break-up. In general, viscous damping is much smaller than the surface tension force and hence the Weber number is the key parameter responsible for break-up. Review of the literature (Ref 22) indicates that the following criteria are widely accepted for droplet break-up:

Regime I: Vibrational break-up; $10\text{-}14 \leq We \leq 40$

Regime II: Atomization with stripping of liquid layer; $40 \leq We \leq 10^3$

Regime III: Rapid catastrophic break-up; $10^3 \leq We \leq 10^4$

For all practical purposes the Weber number of about 14 (Ref 23) can be chosen from the literature as the critical value below which the droplets may deform but do not undergo break-up.

For modeling the droplet break-up, the Taylor Analogy Break-up (TAB) model (Ref 24) can be utilized. This model is briefly summarized here. It assumes that the droplets behave analogous to an oscillating spring mass system with the external loading simulated by the aerodynamic drag, restoring forces being the surface tension, and the viscous damping forces. Equation for an oscillating droplet analogous to a spring mass system is (Ref 25) written as,

$$F_{\text{inertia}} - G_{\text{ST}} x - G_{\text{viscous}} \frac{dx}{dt} = m_{\text{d}} \frac{d^2 x}{dt^2} \tag{Eq 3}$$

where,

$$F_{\text{inertia}} = m_{\text{d}} C_{\text{F}} \frac{2\rho_{\text{p}}(\Delta u)^2}{\rho_{\text{d}} d}; \quad G_{\text{ST}} = m_{\text{d}} \frac{8 C_{\text{k}} \sigma}{\rho_{\text{d}} d^3}; \quad G_{\text{viscous}} = m_{\text{d}} \frac{4 C_{\text{d}} \mu_{\text{d}}}{\rho_{\text{d}} d^2} \tag{Eq 4}$$

C_{F}, C_{k}, and C_{d} are constants having values of 1/3, 8, and 5, respectively (Ref 25, 26). Break-up is assumed to occur when the distortion x is $x \geq 0.5d$ as suggested in Ref 27. Equation 3 is nonhomogeneous second-order ODE with the inertial term that depends on the relative velocity that requires the plasma velocity field to be known. The size of the child droplets is determined by equating the energy of the parent droplet to the combined energy of the child droplets. More details about the TAB model can be found in Ref 24 and 25.

The process of droplet break-up occurs in a time scale of the order of microseconds and as such droplet heating and vaporization are not considered in detail at this stage. The droplet temperature variation in this time frame is modeled rather simply based on the lumped capacity analysis as,

$$m_{\text{d}} C_{\text{p,d}} \frac{dT_{\text{d}}}{dt} = h A_{\text{droplet}} (T_\infty - T_{\text{d}}) + \frac{dm_{\text{d}}}{dt} h_{\text{lv}} \tag{Eq 5}$$

where T_∞ is the plasma temperature around the droplet, T_{d} is the droplet temperature, and $A_{\text{droplet}} = \pi d^2$ is the surface area of the droplet. The heat transfer coefficient is evaluated using correlation of Ranz and Marshall (Ref 28)

$$Nu \equiv \frac{hd}{k_\infty} = 2.0 + 0.6 Re_d^{1/2} Pr^{1/3} \quad \text{(Eq 6)}$$

where $Re_d = \rho_\infty d \Delta u / \mu_\infty$ is the Reynolds number and Pr is the Prandtl number. In the break-up analysis, the effect of droplet surface temperature on surface tension was varied parametrically in assessing its influence on droplet break-up in the results section.

2.2 Droplet Heat-up, Vaporization, and Internal Precipitation

In this study, it is realized that the aerodynamic processes of very short timescale have already produced droplets of stable sizes that will not undergo further break-up. All the droplets introduced into the plasma undergo rapid heating resulting in solvent vaporization and increased concentration of solute near the droplet surface. At a critical value of solute concentration, precipitation occurs resulting in the formation of a porous shell around the liquid core. The precipitation leading to shell formation is assumed to be instantaneous based on the supersaturation concentration value of solute based on the data in the literature (Ref 17). This part of the model is abstracted from our earlier work (Ref 10) except that the internal recirculation within the droplet due to shear at the liquid-gas interface has been neglected. This simplification leads to spherically symmetric concentration and temperature distributions within the droplet and thus does not account for the fore-to-aft variations within the droplets. The binary (solute + solvent) droplets are assumed to be injected axially or transversely into a high-temperature plasma jet where solvent portion of the droplet vaporizes with simultaneous reduction in droplet size and increase in the solute concentration. The droplets are assumed to be composed of zirconium acetate (solute) dissolved in liquid water (solvent) with a prescribed initial zirconium acetate mass fraction. Droplet motion in the hot convective gas environment is governed by the droplet momentum equation given by,

$$\frac{\partial U}{\partial t} = \frac{3 C_D}{8 r_s} \frac{\rho_\infty}{\rho_L} |U_\infty - U| (U_\infty - U) \quad \text{(Eq 7)}$$

$$\frac{\partial V}{\partial t} = \frac{3 C_D}{8 r_s} \frac{\rho_\infty}{\rho_L} V^2 \quad \text{(Eq 8)}$$

where U and V are the droplet velocities in x and y directions, respectively, and C_D is the drag coefficient due to the relative motion between the droplet and the surrounding hot gases with U_∞ being the streamwise local plasma flow velocity. The change in the droplet radius is given by,

$$\frac{dr_s}{dt} = -\frac{\dot{m}}{4\pi \rho_L r_s^2} \quad \text{(Eq 9)}$$

where $\dot{m}$ is the mass rate of vaporization, ρ_L is the liquid density, and r_s is the radius of the droplet. The drag coefficient, C_D is modified for the surface blowing effects. Under these assumptions, the conservation of solute mass and energy equations can be written in nondimensional forms as,

$$Le_L \bar{r}_s^2 \frac{\partial \bar{\chi}}{\partial \tau} - 0.5 Le_L \frac{dr_s}{dt} \eta \frac{\partial \bar{\chi}}{\partial \eta} = \frac{1}{\eta^2} \frac{\partial}{\partial \eta} \left(\eta^2 \frac{\partial \bar{\chi}}{\partial \eta} \right) \quad \text{(Eq 10)}$$

$$\bar{r}_s^2 \frac{\partial \bar{T}}{\partial \tau} - 0.5 \frac{dr_s}{dt} \eta \frac{\partial \bar{T}}{\partial \eta} = \frac{1}{\eta^2} \frac{\partial}{\partial \eta} \left(\eta^2 \frac{\partial \bar{T}}{\partial \eta} \right) \quad \text{(Eq 11)}$$

where following dimensionless quantities are employed $\bar{r}_s = r_s/r_0$, $\tau = \alpha_L t / r_0^2$, $\eta = r/r_s$, $\bar{\chi} = (\chi - \chi_0)/\chi_0$, and $\bar{T} = (T - T_0)/T_0$, with r_0 is the initial radius, α_L is the liquid thermal diffusivity, t is time, r_s is the droplet surface radius, T is temperature with T_0 being the initial value, and correspondingly χ being the solute mass fraction with χ_0 being its initial value. Le_L is the liquid phase Lewis number defined as D_s/α_L. The initial and boundary conditions for the droplet can be written as,

$$\left\{ \begin{matrix} \bar{\chi} \\ \bar{T} \end{matrix} \right\} (\tau = 0) = 0 \text{ and } \frac{\partial}{\partial \eta} \left\{ \begin{matrix} \bar{\chi} \\ \bar{T} \end{matrix} \right\} \Bigg|_{\eta=0} = 0 \text{ and } \frac{\partial}{\partial \eta} \left\{ \begin{matrix} \bar{\chi} \\ \bar{T} \end{matrix} \right\} \Bigg|_{\eta=1} = \left\{ \begin{matrix} \frac{\dot{m}}{4\pi r_s \rho_L D_s \chi_{z,0}} \\ \frac{\dot{Q}_L}{4\pi r_s k_L T_0} \end{matrix} \right. \quad \text{(Eq 12)}$$

where $\dot{Q}_L$ is the heat flux to the droplet, k_L is the liquid conductivity, ρ_L is liquid density, and D_s is the mass diffusivity of solute in solvent.

2.3 Internal Vaporization and Pressurization

The model detailed above describes the physical processes until the onset of precipitation and formation of a precipitate shell. Subsequent to shell formation, further heating of the particle containing a liquid core is modeled as follows. The particle motion through the hot plasma is still governed by Eq 7 and 8 except that the particle size is now fixed to the outer diameter of the precipitate shell. The Nusselt number for the porous and nonporous shells are obtained as described in Basu and Cetegen (Ref 29). The model for the particle interior is divided into three zones: solid shell, liquid core, and vapor annulus as schematically shown in Fig. 4. In each region, the energy equation is of the same form as Eq 11 with a moving interface between the liquid core and the vapor film. The enthalpy carried by the vapor escaping through the pores is accounted for in the model as detailed in Basu and Cetegen (Ref 29). Depending on the type of shell formed, one may or may not have any venting effect through the pores in the shell. However, for the general case of a shell of porosity ε, one can write the following mass balance equation for the vapor.

$$\dot{m}_v = -\dot{m}_l - \dot{m}_{out} \quad \text{(Eq 13)}$$

where the $\dot{m}_v$ is the vapor mass generation rate within the shell, $\dot{m}_l$ is the rate of change remaining core liquid mass, and $\dot{m}_{out}$ is the rate of vapor mass leaving the porous shell. After some algebraic manipulations with the ideal gas law assumption, this reduces to:

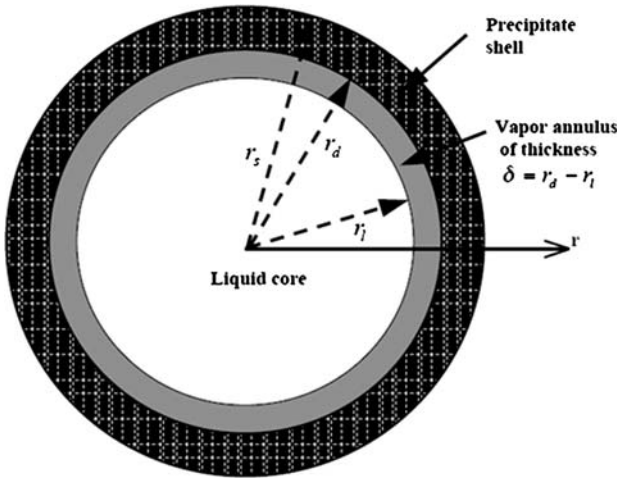

Fig. 4 Schematics of the droplet after precipitation

$$\frac{dp_v}{dt} = \frac{RT_v}{V_v}\left[4\pi r_l^2 \rho_v \left|\frac{dr_l}{dt}\right| - 4\pi r_l^2 \rho_l \frac{dr_l}{dt} - \rho_v A_{pore} V_{pore}\right] \quad \text{(Eq 14)}$$

where V_{pore} is the velocity of the gas venting through the pores of the shell estimated from Karman-Cozeny equation while A_{pore} is the total area of the pores. ρ_v and ρ_l denote the densities of the vapor and liquid phase while r_l is the radius of the liquid core. Equation 14 gives an expression for internal pressure rise as a function of the vapor velocity escaping through the pores and the rate at which the liquid front is receding towards the droplet center.

Internal pressurization of the shell due to vaporization of the liquid within it can lead to shell rupture or inflation depending on the shell type that forms during precipitation. This obviously depends on the solute and solvent characteristics and the thermo-physical conditions under which the precipitation occurs. Considering the case of a solid precipitate shell, the simplest shell fracture criterion is the failure stress of the shell material. In this approach, the fracture criterion becomes,

$$p_v = \frac{2\delta\sigma}{r_s} \quad \text{(Eq 15)}$$

where σ represents the failure stress of the shell material and δ is the shell thickness. While, it is difficult to prescribe the failure stress of a precipitate shell, which may depend on a multitude of parameters, some estimates based on published pure solute oxide (such as zirconium oxide) failure stresses are useful to study the possible outcomes.

3. Results and Discussion

In the preceding description of the models, plasma velocity and temperature fields are needed. In this study, plasma flow field was modeled as a high-temperature turbulent jet originating from a 8 mm diameter nozzle at a velocity and temperature of 600 m/s and 10,000 K, respectively. These values were based on the measurements by Semenov and Cetegen (Ref 30). The experimental data were obtained using a METCO 9 MB DC-arc plasma torch. The plasma gas medium was an Argon-hydrogen mixture with Argon mole fraction of 0.8 at an input power of 24 kW and gas flow rate of 3.6 m^3/h. The plasma thermal efficiency was determined to range between 55 and 60%. Semenov and Cetegen (Ref 30) utilized a two-region approach to measure the plasma velocity. In the luminous zone of the plasma near the nozzle exit, they used high-speed imaging to determine the convective velocities while in the less luminous regime away from the plasma core, laser Doppler anemometry was utilized to measure flow velocities. Figure 5 displays the temperature and velocity decay along the plasma jet axis. It is seen that the temperature drops to 20% of its inlet value within a distance of 14 diameters from the nozzle exit as shown in Fig. 5(a). The experimental data obtained from emission spectroscopy match the computations reasonably well within 3 diameters distance from the nozzle exit. Similar degree of agreement was found for the velocity comparison as shown in Fig. 5(b). Because of the low Reynolds number of the plasma jet at the plasma nozzle exit without accounting for the arc-generated turbulence, the plasma jet was also computed as a steady laminar jet for comparison. It was found, however, that the decay rate of both temperature and axial velocity along the centerline of the jet was significantly slower for the laminar case and they did not follow the experimental data as seen in Fig. 5. This suggests that the droplets injected into an unrealistic laminar plasma jet experience a significantly higher velocity and higher temperatures compared to the more realistic turbulent jet.

In the following, we first present droplet break-up results based on the TAB model described earlier. This is followed by results from droplets undergoing precipitation, shell formation, and possible disintegration due to internal pressurization. The guidelines obtained from the modeling effort are then projected to those for obtaining different types of coating morphologies.

3.1 Aerodynamic Break-up Results for Axial Injection

In the case of axial injection, droplets were injected into the plasma flow at a velocity of 15 m/s along the axis of the nozzle. The initial temperature of the droplets was assumed to be 300 K. Figure 6 shows the droplet diameter variation with downstream axial distance for an initial size of 50 microns. It is found that the droplets injected into the laminar plasma jet undergo rapid heating and vaporization in a short distance from the plasma exit due to higher sustained temperatures in the laminar plasma jet potential core. For the turbulent plasma jet, similar droplet diameter reductions take longer distances primarily as a result of the influence of turbulent mixing on plasma jet temperature decay. It is found that 50 micron

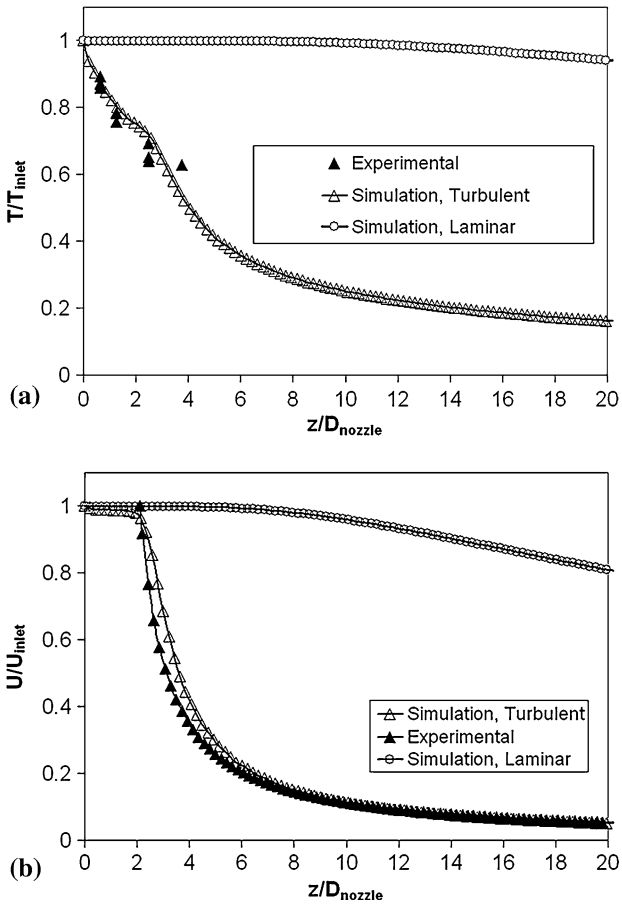

Fig. 5 (a) Experimental and computational temperature profiles along the axis of the jet normalized by the inlet temperature. (b) Experimental and computational velocity profiles along the axis of the jet normalized by the inlet velocity

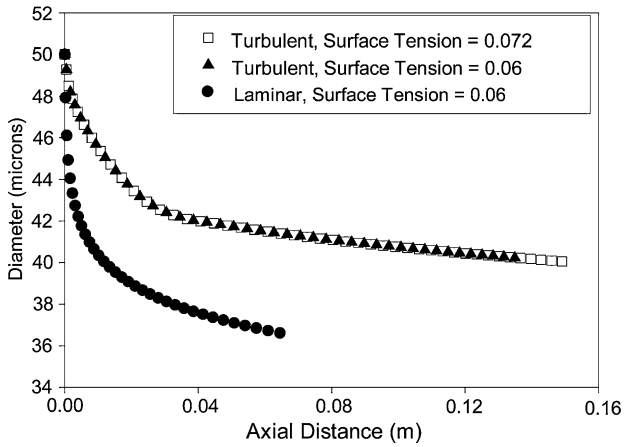

Fig. 6 Variation of droplet diameter with axial distance for a 50 micron initial diameter droplet for different levels of surface tension for laminar and turbulent plasma flow fields

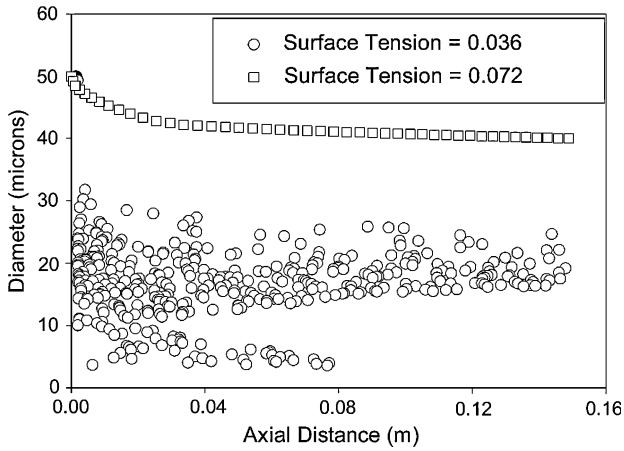

Fig. 7 Aerodynamic breakup of 50 micron initial diameter droplets for a surface tension of 0.036 N/m in a turbulent plasma

droplets do not experience aerodynamic break-up in either case. Since the surface tension of the precursor droplet is estimated to vary from 0.072 N/m to 0.06 N/m for a temperature change of 90 °C at the surface of the droplet, simulations were performed using both values. It is apparent that this reduction in surface tension is not sufficient to initiate droplet break-up.

Figure 7 reveals the influence of further reducing the surface tension by means of surfactant addition, for example. In this case, a reduction of surface tension by a factor of two from the nominal value of 0.072 N/m becomes sufficient to cause droplet break-up. The unstable droplets undergo break-up within 0.5-1.0 μs of injection resulting in the formation of smaller droplets having a diameter range from 5 to 30 microns. This degree of size reduction is much larger than what can be obtained by evaporation. The aerodynamic break-up is principally responsible for large reductions in droplet size as well as its dispersion over a range of sizes. The actual droplet size distribution is dependent on the oscillation mode and ratio of the total energy (in distortion and oscillation) to the energy in the fundamental oscillation mode. Coupling with the turbulent fluctuations of the plasma jet also affects the droplet size. A single droplet may also undergo breakup into more than two droplets. However, the overall droplet size dispersion is a combined effect of both droplet break-up and vaporization.

Figure 8 shows the role of surface tension in the final size distribution of droplets after break-up. For a four times reduction of surface tension, the droplet diameters after break-up are less than 21 microns. Reduction of surface tension to 0.018 N/m makes the droplets significantly more unstable leads to significant degree of droplet break-up. Figure 9 illustrates the marginal case where a small reduction in surface tension can lead droplets from stable to the unstable regime. 70 micron droplets fall in the neutral stability region where a small shift in the surface tension can induce break-up. Based on the findings for the 70 micron droplet, surface tension values of 0.06 and 0.072 N/m correspond to the values above and below the critical Weber numbers for break-up. Weber numbers for both cases of 70 micron droplet are $We(\sigma = 0.06) = 14$

and $We(\sigma = 0.072) = 11.7$. Analysis of TAB model results for different size droplets and surface tension values lead to the result that any droplet with a Weber number greater than 14 would undergo break-up. This value also corresponds to the critical Weber number reported in the literature (Ref 23). According to this criterion, a 20 micron droplet would undergo break-up at a surface tension value of 0.017 N/m. Similarly, it is shown that 50 micron droplets with surface tension values of 0.036 and 0.018 N/m would experience break-up since the corresponding Weber numbers are 16.7 and 33.3, respectively. Figure 10 shows that 110 micron axially injected droplet is unstable for a surface tension value of 0.072 N/m. It is found that the Weber number for the 110 micron droplet is approximately 19, which lies in the unstable regime. Figure 11 depicts that increasing surface tension value by a factor of 4 stabilizes large droplets. It is found that the Weber number for a 110 micron droplet with a surface tension value of 0.29 N/m is 4.75, which is below the critical Weber number value. The only diameter reduction is due to the evaporation of solvent from the droplet surface in the case of no aerodynamic break-up.

Figure 12 shows the axial velocities for 110 micron droplets. Velocities show rapid acceleration within a very short distance from the nozzle exit followed by a gradual deceleration. This is the expected behavior based on the initial droplet acceleration in the high-velocity jet followed by their equilibration to the local plasma jet conditions downstream. Since the plasma velocity field decays with axial distance from the nozzle exit, droplets follow the decay pattern of the jet itself. The dispersion of droplet axial velocities is a result of the fact that the smaller size droplets are able to attain higher velocities whereas the larger droplets cannot accelerate as much, leading to a range of droplet velocities at a given axial location.

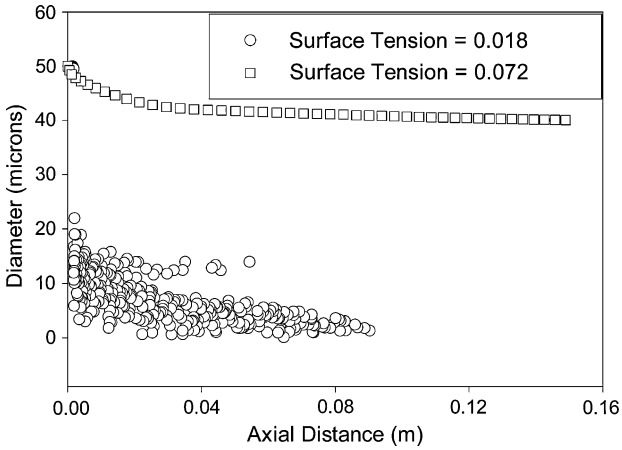

Fig. 8 Aerodynamic breakup of 50 micron initial diameter droplets for a surface tension of 0.018 N/m in a turbulent plasma

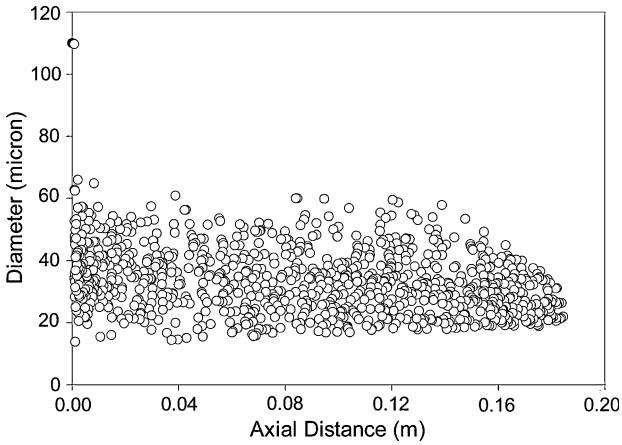

Fig. 10 Aerodynamic breakup of 110 micron initial diameter droplets for a surface tension of 0.072 N/m

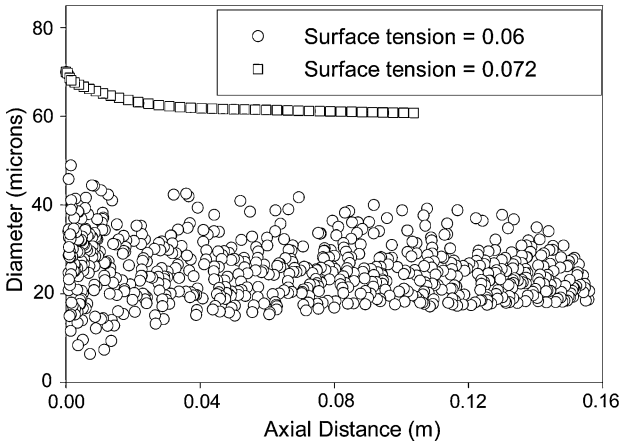

Fig. 9 Aerodynamic breakup of 70 micron initial diameter droplets for a surface tension of 0.06 N/m. No breakup is detected for 0.072 N/m surface tension

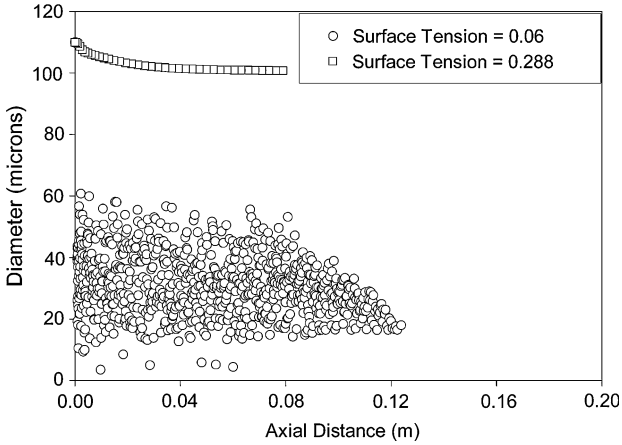

Fig. 11 Aerodynamic breakup of 110 micron initial diameter droplets for surface tensions of 0.06 N/m. Same sized droplet with surface tension value of 0.288 N/m shows no break-up

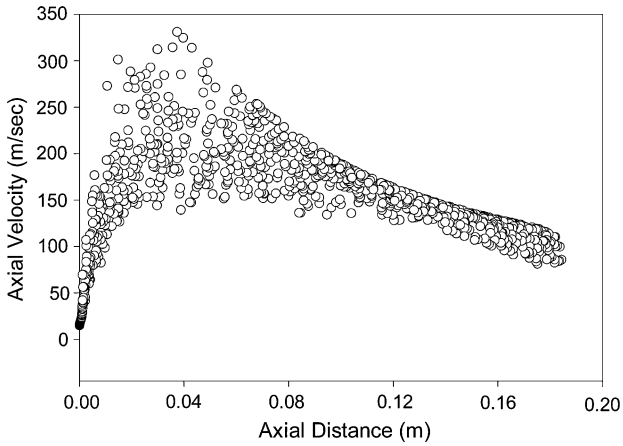

Fig. 12 Axial velocity profile for a 110 micron axially injected droplet with surface tension of 0.072 N/m

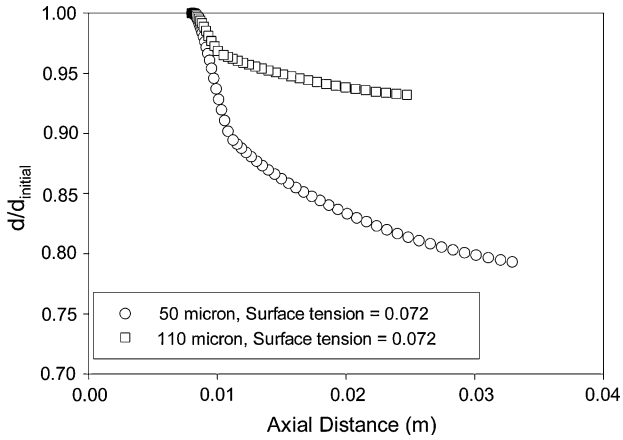

Fig. 13 Variation of droplet with axial distance for 50 and 110 micron initial diameter droplets injected transversely into the plasma

3.2 Aerodynamic Break-up Results for Transverse Injection

In the transverse injection scheme, the droplets are injected normal to the plasma flow at an axial distance of 8 mm downstream of the nozzle exit and offset radially by 12 mm from the plasma jet centerline. The radial injection velocity of droplets was 12 m/s while their initial temperature was assumed to be 300 K. Transversely injected droplets initially pass through the cooler, lower velocity edge of the plasma jet. Consequently, the Weber numbers of these droplets invariably fall below the critical value even for large droplet sizes like 110 microns. This is because the Weber number scales as $(\Delta u)^2$. Hence for downstream injection, droplets encounter a much lower gas-phase velocity magnitude. This is evident in Fig. 13 where even the 110 micron droplets do not undergo break-up. Figure 14 shows that droplet break-up can occur for sufficiently large droplet sizes such as 140 microns. Since the typical size distribution of transversely injected droplets in the solution precursor plasma spray (SPPS) process is less than 100 microns, it is anticipated that aerodynamic break-up is an unlikely occurrence preceding the vaporization, precipitate formation, and rupture. Table 1 provides a summary of the aerodynamic break-up of the droplets of various sizes and surface tensions. It should also be mentioned that while the Weber number break-up criterion predicts the likelihood of aerodynamic break-up, it does not provide any information of the size of the droplets upon break-up. The TAB model provides this information and is useful in that context. The prediction of the produced droplet sizes from the TAB model were compared with the simple expression given by Fauchais et al. (Ref 31). The agreement was found to be remarkably good given the simplicity of the expression and the differences in the two models.

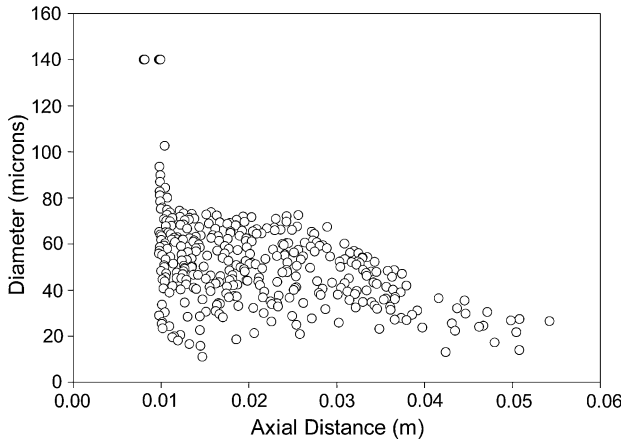

Fig. 14 Aerodynamic breakup for 140 micron initial diameter droplets injected transversely into the plasma

Table 1 Stability regimes for shear break-up of droplets

	Surface tension, N/m				
	0.072	**0.06**	**0.036**	**0.018**	**0.288**
Laminar axial, micron					
50	NB	NB	B	B	NB
110	B	B	B	B	NB
Turbulent axial, micron					
50	NB	NB	B	B	NB
70	NB	B	B	B	NB
110	B	B	B	B	NB
Turbulent transverse, micron					
50	NB	NB			
110	NB	NB			
140	B	B			

B: Breakup, NB: No breakup, $We_{critical} = 14$

3.3 Results on Precipitate Formation

From the aerodynamic break-up analysis, the typical droplet diameters range between 5 and 45 microns for the injection methodologies studied here. As a result, droplets of four different sizes (5, 10, 30, and 40 microns) were

studied for thermo-physical transformations in the plasma field. Upon being injected into the plasma flow field, droplets undergo heating and vaporization leading to decreasing droplet sizes and increase in the concentration of the solute (zirconium acetate in this case) near the droplet surface. Precipitation is triggered as soon as the surface concentration of the solute exceeds a supersaturation mass fraction of 0.95 for zirconium acetate. The precipitation is assumed to be instantaneous and all parts of the droplet with mass fraction of solute greater than the saturation mass fraction are assumed to precipitate forming a shell around the droplet with a liquid core. The precipitated droplet continues to be heated by the plasma leading to the formation of a vapor annulus around the liquid core, which pressurizes the droplet and causes it to shatter.

Figure 15 shows the variation of temperature and solute mass fraction in a 5 micron diameter droplet injected axially into the plasma flow field for initial solute mass fractions of 0.2, 0.4, and 0.6, respectively. In all cases, temperature varies little within the droplet with an increase towards the droplet surface. Solute concentration varies significantly more from center to the outer surface of the droplet as a result of lower mass diffusivity of solute as compared to much larger thermal diffusivity. Droplet with an initial solute mass fraction of 0.6 precipitates earliest while the longest precipitation time is expected for a droplet with initial mass fraction of 0.2. For this and all other droplet sizes considered, temperature is almost constant within the droplet as the thermal equilibration timescale is short and virtually independent of the precipitation timescale. It is also seen that the radial solute mass fraction profile is more uniform for the droplet with initial solute mass fraction of 0.6 and progressively becomes steeper for lower initial solute mass fraction levels. For 5 micron droplet, precipitation regions for all the initial solute levels encompass the entire droplet, thus creating solid particles.

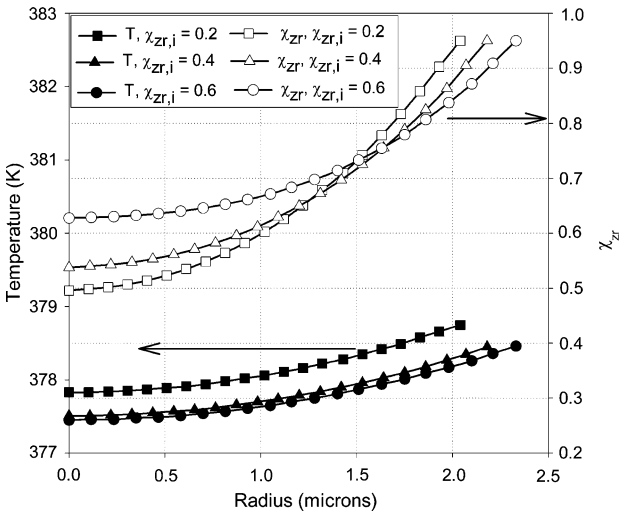

Fig. 15 Variation of mass fraction and temperature within 5 micron for initial solute mass fractions of 0.2, 0.4, and 0.6

Similar results are shown for 10 micron droplets in Fig. 16. Similar trends are observed with respect to the gradients of the solute concentration profiles. However, the shell thicknesses for the 0.4 and 0.2 initial solute mass fraction droplets are almost the same around 4.4 micron with respect to the final outer diameter of 8.4 microns. The droplet with a solute mass fraction of 0.6 precipitates as a solid particle since the equilibrium saturation mass fraction is about 0.56. Similar behavior was observed for both 30 and 40 micron droplets shown in Fig. 17 and 18. In both cases, the gradient of the solute concentration profiles decreases with increasing initial solute mass fraction. The timescale of precipitation is significantly longer than the 5 and 10 micron droplets. As expected, the timescale of precipitation decreases with increasing initial solute level. Both 30 and 40 micron droplets form thin shells of thicknesses varying from 1.5 to 2 microns. These droplets are expected to have a large liquid core surrounded by a thin shell, which may be porous. It is also found that droplets having initial solute mass fractions of 0.2 and 0.4 precipitate into shells of about the same thickness.

3.4 Internal Pressurization of Precipitates

Modeling of droplet vaporization and precipitation presented above suggests that 5 micron droplets precipitate into solid particles while larger 10-40 micron droplets

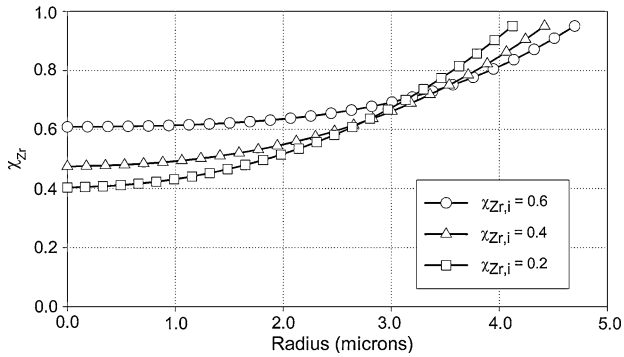

Fig. 16 Variation of mass fraction and temperature within 10 micron for initial solute mass fractions of 0.2, 0.4, and 0.6

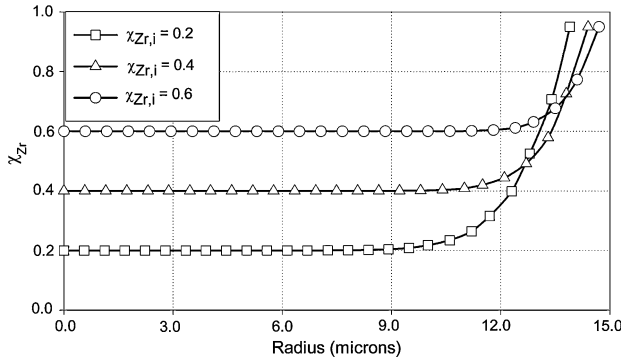

Fig. 17 Variation of mass fraction and temperature within 30 micron for initial solute mass fractions of 0.2, 0.4, and 0.6

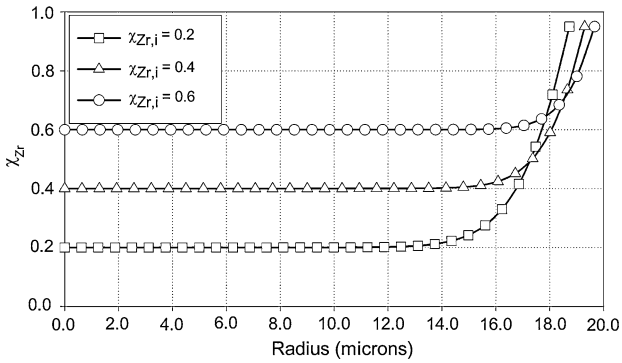

Fig. 18 Variation of mass fraction and temperature within 40 micron for initial solute mass fractions of 0.2, 0.4, and 0.6

form thick and thin precipitate shells, respectively. The postprecipitation analysis is done for 10 micron and 40 micron droplets only. The results from the precipitation model are provided as input to the thermal model to predict internal pressurization. The plasma velocity and temperature fields are sampled as the particle continues along its trajectory to calculate the heat transfer into the particle. Figure 19(a) shows the internal pressure rise for a 10 micron initial diameter droplet for the impervious shell and two levels of porosity. It is seen that the internal pressure rise is the fastest for the impervious shell since the impervious shell does not allow escape of any vapor from the particle. A small initial but rapid pressure rise occurs due to formation of the vapor layer between the liquid core and the shell. This is followed by continuous rise of pressure due to vaporization within the shell. For 20% porosity of the shell, the rate of pressure rise is reduced as compared to the impervious shell case due to venting of the formed vapor from the shell. For 40% shell porosity, the rate of pressure rise is much smaller after a relatively constant pressure period where rates of vapor generation and escape from the shell are similar. In all cases, the internal pressure rise occurs over a period of microseconds as compared to the time scale of precipitate formation of milliseconds indicating three orders of time separation between the two processes. Once the precipitate shell forms, the subsequent internal pressurization is almost instantaneous. Figure 19(b) also shows that a rapid small pressure rise occurs initially followed by a more gradual increase depending on the porosity level for a 40 micron particle. It is also observed that the pressure decay occurs in the early part of the process particularly for the porous shells. This is due to the fact that during the early stage the shell is not heated sufficiently enough to trigger a significant phase change in the liquid core leading to negligible pressure rise. However, as the rate of liquid front shrinkage increases, the rate of pressure rise overcomes the venting effect of the vapor through the pores. Inspection of Eq 14 suggests that if the last term on the right-hand side is larger than the combined sum of the first two terms at early times when dr_f/dt is very low, in which case the pressure gradient may become negative. This is what happens with increasing porosity as the vapor mass

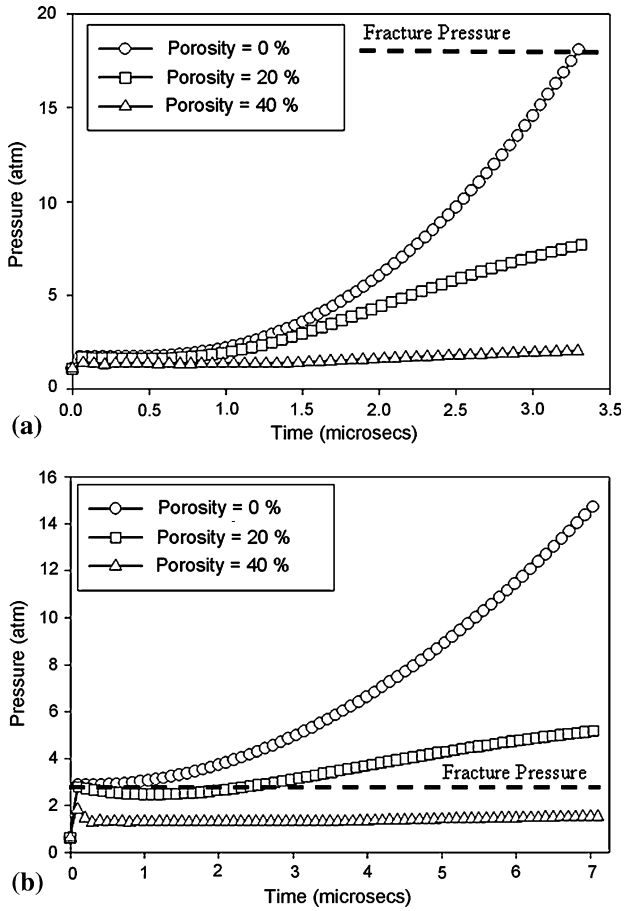

Fig. 19 Internal pressure rise inside (a) 10 micron, (b) 40 micron for different levels of porosity. Initial solute mass fraction is 0.2. Fracture criteria is set at 20 atm for 10 micron droplets and 15 atm for the 40 micron droplet

flux through the pores increases. The trends are similar with the 10 micron droplet case except that the pressure rise occurs more slowly for the larger droplet.

The main objective of calculating the internal pressure rise is to determine if and when the shell would fracture due to internal pressurization. While there is no quantitative data on the failure stress for the shell material, which may or may not be porous, an estimate of this can be made using the failure strength of amorphous zirconia, the shell material. Based on the values reported in the literature for the failure strength (σ = 2-3 MPa), the internal pressure at which fracture is expected can be calculated from Eq 15. Fracture occurs at an internal pressure of 20 atm for the smallest droplet and decreases with the shell thickness relative to the droplet size. For the 40 micron droplet, an internal pressure of 15 atm can be used as a conservative estimate for fracture to occur while for a 10 micron droplet, the internal pressure rise is allowed to be 20 atm before the shell fragments. Physically, it is obvious that the porous shells will be weaker than a non-porous shell but due to the lack of experimental data, the same value is taken to be the fracture pressure for all the cases irrespective of porosity.

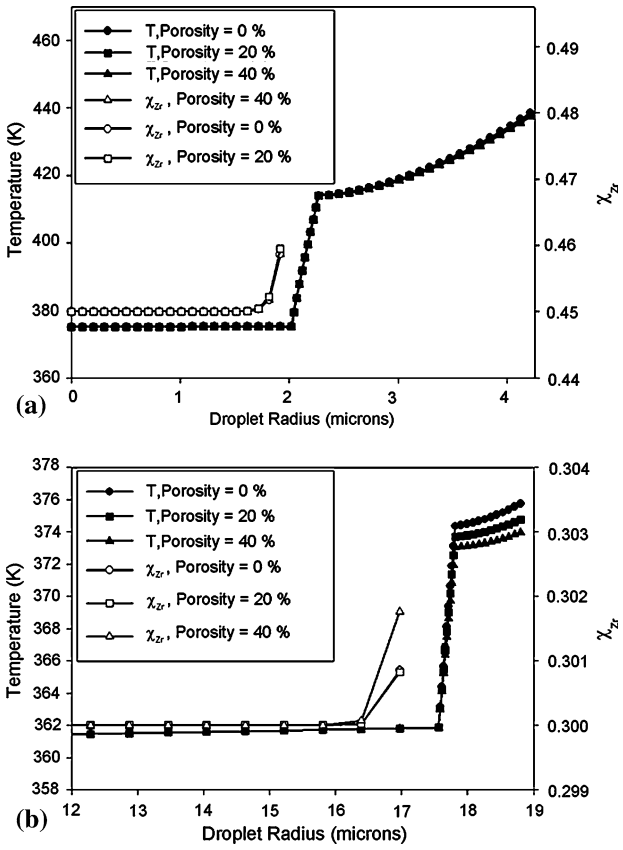

Fig. 20 Temperature and zirconia mass fraction variation with radius for (a) 10 micron and (b) 40 micron droplet for different levels of porosity

Figure 20 shows the radial distributions of temperature and solute mass fraction for different levels of porosity for 10 and 40 micron droplets. It is seen that the profiles for all levels of porosity for a 10 micron droplet are similar as shown in Fig. 20(a). There is a significant temperature drop in the solid shell and a larger drop in the vapor film due to its low thermal conductivity. However, in the small time scale of this pressurization process, the temperature of the liquid core rises by only 0.2 °C as indicated by the temporal history of temperature near the vapor-liquid interface. Most parts of the liquid core remains at the initial condition and is shielded from the heat of the plasma by the solid shell and the vapor layer. The mass concentration profiles show a rise at the liquid-vapor interface by about 0.010 from the base value of 0.45. Similar trends are seen in Fig. 20(b) for a 40 micron droplet. The increase in mass concentration near the surface is about 0.02 for droplets of sizes of 20 and 40 microns.

4. Summary

The model descriptions and the results described above provide a detailed analysis of the possible thermo-physical phenomena that occur at the droplet scale. The final microstructure of the coatings is determined by combination of the physics described by the three distinct phases of the model. For example, in aerodynamic break-up, any droplet that is over a certain initial size disintegrates and forms a variety of smaller droplets. This break-up can even be fostered in smaller droplets if the surface tension can be reduced by the use of surfactants for example. The smaller droplets have lower inertia and are more easily entrained into the plasma. Better entrainment and heat-up of droplets would lead to better pyrolization and deposition of coatings with smaller amount of unpyrolized material. This suggests that controlling the aerodynamic break-up of droplets injected into plasma can be important. This can be achieved by increasing the droplet size, reducing the surface tension or by axial injection of droplets through the core of the plasma jet. The model results serve as guidelines on the relative importance of each of these processes. The second part of the model shows that smaller droplets are not only better entrained but tend to volume precipitate. This volume precipitation and subsequent intense heating usually results in molten splats on the substrate resulting in denser coatings.

Large droplets typically form shell type precipitates, which are detrimental to the final coating quality as they may be embedded as unmolten fragments in the coating. Precipitation characteristics also depend on the initial solute loading. Higher initial solute loading increases the precipitate shell thickness. Once formed, the shell may experience internal pressurization, and depending on shell porosity, undergo fragmentation by exposing the internally trapped liquid to high-temperature plasma. The liquid core may split into two or more small droplets. These droplets may traverse radially outward to the colder zones of the plasma jet and heated poorly arriving at the substrate in unpyrolized or semipyrolized form degrading the coating quality.

The modeling presented in this article captures most of the relevant physics and can be used as guide for design and optimization of solution plasma spray process parameters. However, there are still significant uncertainties in the droplet level processes (for instance, precipitation onset and progress) that need experimental confirmation.

Acknowledgments

The work presented in this article was financially supported by the Office of Naval Research Grant No. N00014-02-1-0171, under the direction of Dr. Larry Kabakoff. We acknowledge our many discussions on the topic with our colleagues, Prof. Maurice Gell (UConn), Prof. Nitin Padture (Ohio State Univ.) and Dr. Chin Ma (Inframat Corporation).

References

1. K. Masters, Spray Drying Handbook (4th ed.). John Wiley & Sons, New York, 1985
2. L. Pawlowski, The Science and Engineering of Thermal Spray Coatings. John Wiley & Sons, Chichester, England, 1995

3. N.P. Padture, K.W. Schlichting, T. Bhatia, A. Ozturk, B.M. Cetegen, E.H. Jordan, and M. Gell, Towards Durable Thermal Barrier Coatings with Novel Microstructures Deposited by Solution-Precursor Plasma Spray, *Acta Mater.*, 2001, **49**, p 2251-2257
4. E.H. Jordan, L. Xie, X. Ma, M. Gell, N.P. Padture, B.M. Cetegen, A. Ozturk, J. Roth, T.D. Xiao, and P.E. Bryant, Superior Thermal Barrier Coatings Using Solution Precursor Plasma Spray, *J. Therm. Spray Tech.*, 2004, **13**(1), p 57-65
5. T. Bhatia, A. Ozturk, L. Xie, E.H. Jordan, B.M. Cetegen, M. Gell, X. Ma, and N.P. Padture, Mechanisms of Ceramic Coating Deposition in Solution-Precursor Plasma Spray, *J. Mater. Res.*, 2002, **17**(9), p 2363-2372
6. N.P. Padture, M. Gell, and E.H. Jordan, Thermal Barrier Coatings for Gas Turbine Engine Applications, *Science*, 2002, **296**, p 280-284
7. A. Ozturk and B.M. Cetegen, Experiments on Ceramic Formation from Liquid Precursor Spray Axially Injected into an Oxy-Acetylene Flame, *Acta Mater.*, 2005, **53**, p 5203-5211
8. B.G. Ravi, S. Sampath, R. Gambino, P.S. Devi, and J.B. Parise, Plasma Spray Synthesis from Precursors: Progress, Issues, and Considerations, *J. Therm. Spray Tech.*, 2006, **15**(4), p 701-707
9. J. Oberste-Berghaus, S. Bouaricha, J.-G. Legoux, and C. Moreau, Injection Conditions and In-Flight Particle States in Suspension Plasma Spraying of Alumina and Zirconia Nano-Ceramics, *Proceedings of the ITSC 2005*, Advances in Technology and Application, ASM International, May 2-4, 2005, Basel, Switzerland, p 512-518
10. A. Ozturk and B.M. Cetegen, Modeling of Plasma Assisted Formation of Yttria Stabilized Zirconia From Liquid Precursors, *Mater. Sci. Eng. A*, 2004, **384**, p 331-351
11. A. Ozturk and B.M. Cetegen, Modeling of Axially and Transversely Injected Precursor Droplets into a Plasma Environment, *Int. J. Heat Mass Tran.*, 2005, **48**(21-22), p 4367-4383
12. A. Ozturk and B.M. Cetegen, Modeling of Axial Injection of Ceramic Precursor Droplets into an Oxy-Acetylene Flame Environment, *Mater. Sci. Eng. A.*, 2006, **422**(1-2), p 163-175
13. I. Castillo and R.J. Munz, Transient Heat, Mass and Momentum Transfer of an Evaporating Stationary Droplet Containing Dissolved Cerium Nitrate in a rf Thermal Argon–Oxygen Plasma Under Reduced Pressure, *Int. J. Heat Mass Tran.*, 2007, **50**(1-2), p 240-256
14. N.A. Fuchs, Evaporation and Droplet Growth in Gaseous Media. Pergamon Press, New York, 1959
15. W.E. Ranz and W.R. Marshall, Evaporation from Droplets, Part II, *Chem. Eng. Prog.*, 1952, **48**, p 173-179
16. G.V. Jayanthi, S.C. Zhang, and G.L. Messing, Modeling of Solid Particle Formation During Solution Aerosol Thermolysis, *Aerosol Sci. Tech.*, 1993, **19**, p 478-490
17. G.L. Messing, S.C. Zhang, and G.V. Jayanthi, Ceramic Powder Synthesis by Spray Pyrolysis, *J. Am. Ceram. Soc.*, 1993, **76**, p 2707-2726
18. S.-C. Zhang, G.L. Messing, and M. Borden, Synthesis of Solid, Spherical Zirconia Particles by Spray Pyrolysis, *J. Am. Ceram. Soc.*, 1990, **73**(1), p 61-67
19. S. Jain, D.J. Skamser, and T.T. Kodas, Morphology of Single-Component Particles Produced by Spray Pyrolysis, *Aerosol Sci. Tech.*, 1997, **27**, p 575-590
20. S. Che, O. Sakurai, K. Shinozaki, and N. Mizutani, Particle Structure Control Through Intraparticle Reactions by Spray Pyrolysis, *J. Aerosol Sci.*, 1998, **29**(3), p 271-278
21. J.-C. Lin and J.W. Gentry, Spray Drying Drop Morphology: Experimental Study, *Aerosol Sci. Tech.*, 2003, **37**, p 15-32
22. B.E. Gelfand, Droplet Break-up Phenomena in Flows with Velocity Lag, *Prog. Energy Combust. Sci.*, 1996, **22**, p 201-265
23. T. Watanabe and K. Ebihara, Numerical Simulation of Coalescence and Break-up of Rising Droplets, *Comput. Fluids*, 2003, **32**, p 823-834
24. G.I. Taylor, The Shape and Acceleration of a Drop in a High Speed Air Stream, *Technical report, In the Scientific Papers of G. I. Taylor*, Ed., G.K. Batchelor, 1963
25. Fluent User Manual for version 6.2.19 [www.fluent.com]
26. H. Lamb, Hydrodynamics (6th ed.). Dover Publications, New York, 1945
27. P.J. O'Rourke and A.A. Amsden, The TAB Method for Numerical Calculation of Spray Droplet Break-up, *SAE Technical Paper* 872089, 1987
28. W.E. Ranz and W.R. Marshall, Jr., Evaporation from Drops, Part I, *Chem. Eng. Prog.*, 1952, **48**(3), p 141-146
29. S. Basu and B.M. Cetegen, Modeling of Thermo-Physical Processes in Liquid Ceramic Precursor Droplets Injected into a Plasma Jet, *Int. J. Heat Mass Tran.*, 2007, **50**(17-18), p 3278-3290
30. S.Y. Semenov and B.M. Cetegen, Spectroscopic Temperature Measurements in dc-Arc Plasma Jets Utilized in Thermal Spray Processing of Materials, *J. Therm. Spray Tech.*, 2001, **10**, p 326-336
31. P. Fauchais, V. Rat, C. Delbos, J.F. Coudert, T. Chartier L. Bianchi, Understanding of Suspension DC Plasma Spraying of Finely Structured Coatings for SOFC, *IEEE Trans. Plasma Sci.*, 2006, **33**(2), p 920-929